Charge distribution in $CsFAPbI_3$ spatially resolved by scanning microwave impedance microscopy

van der Werf, Verena M.; Zhao, Jiashang; Koning, Jim S.; Nespoli, Jasmeen; Thieme, Jos; Bus, Marcel; Savenije, Tom J.

DOI
10.1016/j.xcrp.2023.101491

Publication date
2023

Document Version
Final published version

Published in
Cell Reports Physical Science

Citation (APA)
van der Werf, V. M., Zhao, J., Koning, J. S., Nespoli, J., Thieme, J., Bus, M., & Savenije, T. J. (2023). Charge distribution in $CsFAPbI_3$ spatially resolved by scanning microwave impedance microscopy. *Cell Reports Physical Science*, *4*(7), Article 101491. https://doi.org/10.1016/j.xcrp.2023.101491

Cell Reports
Physical Science

Article

Charge distribution in $CsFAPbI_3$ spatially resolved by scanning microwave impedance microscopy

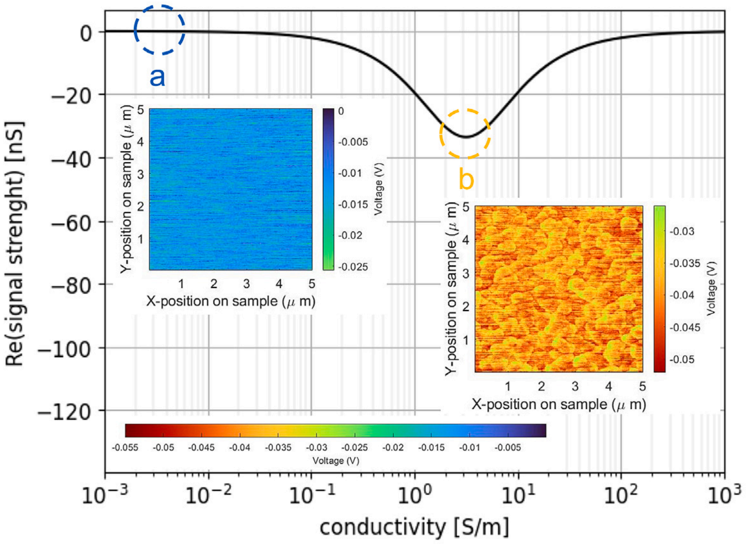

Scanning microwave impedance microscopy is a non-contact, near-field method used to reveal the local conductivity induced by optical illumination in perovskites. For $CsFAPbI_3$, Werf et al. report that excess charges are distributed evenly over grains, but due to local defect-rich areas, possibly related to different crystal facets, local perturbations in carrier concentration exist.

Verena M. van der Werf, Jiashang Zhao, Jim S. Koning, Jasmeen Nespoli, Jos Thieme, Marcel Bus, Tom J. Savenije

t.j.savenije@tudelft.nl

Highlights

sMIM allows local electrodeless measuring of conductivity in semiconductor layers

In situ optically excited charges evenly distribute over $MAPbI_3$ grains

Inhomogeneous carrier distribution in $CsFAPbI_3$ with non-preferred orientation

van der Werf et al., Cell Reports Physical Science 4, 101491
July 19, 2023 © 2023 The Author(s).
https://doi.org/10.1016/j.xcrp.2023.101491

Cell Reports
Physical Science

CellPress
OPEN ACCESS

Article

Charge distribution in $CsFAPbI_3$ spatially resolved by scanning microwave impedance microscopy

Verena M. van der Werf,[1] Jiashang Zhao,[1] Jim S. Koning,[1] Jasmeen Nespoli,[1] Jos Thieme,[1] Marcel Bus,[1] and Tom J. Savenije[1,2,*]

SUMMARY

Metal-halide perovskites deposited by wet-chemical deposition have demonstrated great potential for various electronic applications, including solar cells. A remaining question is how light-induced excess charges become distributed over such polycrystalline material. Here, we examine the local conductive properties of $MAPbI_3$ and $CsFAPbI_3$ by using scanning microwave microscopy (sMIM) in the dark and light. sMIM is an atomic force microscopy (AFM)-based technique measuring variations of the in-phase and out-of-phase signals due to changes in the tip-sample interaction, yielding MIM-Re and MIM-Im images, respectively. Combining this information leads to a picture for $CsFAPbI_3$ in which excess charges are distributed evenly over the grains, but due to local defect-rich areas, possibly related to different crystal facets, local perturbations in carrier concentration exist. For solar cells, this distribution in carrier concentration under illumination leads to variation in the local Fermi level splitting, which should be suppressed to reduce the voltage deficit.

INTRODUCTION

Metal-halide perovskites (MHPs) have demonstrated great potential for various electronic applications including solar cells, LEDs, and X-ray detectors.[1–3] The band gap of these materials can be tuned over a broad range within the visible and near-infrared (NIR) part of the solar spectrum. Moreover, the respectable mobilities and charge carrier lifetimes ensure diffusion lengths substantially exceeding the light penetration depth such that even charges generated far from the MHP/transport layer interface can still efficiently be transported and extracted. Most remarkably, high-quality layers can be deposited by simple wet-chemical deposition techniques, yielding devices with a reported power conversion efficiency above 25%.[4,5] Despite this simple and versatile processing method, the concentrations of trap states are very modest, which is attributed to the fact that most defects do not form a deep state within the optical band gap.[6–8] However, detailed analyses of photovoltaic devices based on these materials show that the maximum attainable voltage has not yet been reached.[9] Part of the voltage deficit is often associated with loss mechanisms at the interface of the MHP with the transport layers.[10,11] This voltage deficit is a result of undesired non-radiative recombination of light-induced charge carriers mediated by, e.g., surface defect states. These could be formed during MHP crystallization and/or on the deposition of the transport layer. Hence, to reduce the voltage deficit, more information regarding these defects is necessary, for instance, their origin, concentration, and spatial distribution over the MHP surface. It is important to realize that a locally high concentration of defect

---

[1]Department of Chemical Engineering, Faculty of Applied Sciences, Delft University of Technology, 2629 HZ Delft, the Netherlands

[2]Lead contact

*Correspondence: t.j.savenije@tudelft.nl

https://doi.org/10.1016/j.xcrp.2023.101491

states leads to a locally lower Fermi level splitting, which reduces the power conversion efficiency (PCE) of the entire solar cell substantially. Hence, a remaining question is how light-induced excess charges spread over such polycrystalline material since an imbalance in concentration might limit the ultimate voltage of a corresponding photovoltaic device.

Over the last few years, a number of nanoscale techniques have been used to study the charge carrier distribution in MHP layers,[12–14] starting with confocal photoluminescence measurements.[14] From those works it was concluded that the grain boundaries are more trap rich than the bulk, resulting in a large heterogeneity in PL intensity.[15] Scanning kelvin probe force microscopy revealed also a large heterogeneity in the contact potential difference, which was at least partially attributed to ion migration occurring on optical excitation.[16,17] Locally recorded I/V curves using photoconductive atomic force microscopy suggested that variations in photovoltage and -current could be linked to dissimilarities in crystal facets.[18] Combination of (time-resolved) local photoluminescence (PL) measurements with other techniques, such as nanodiffraction measurements and transmission electron microscopy (TEM), showed that grains might comprise multiple smaller grains with a spread in crystal orientation, complicating the optoelectronic properties of these materials even more.[19,20] Moreover, defect states limiting the photovoltaic performance turned out to be grouped in clusters.[21]

Despite these insights, it is unclear to what extent excess charge carriers still get evenly spread over the MHP surface. To address this question, we use in this work scanning microwave impedance microscopy (sMIM) to reveal the local conductivity induced by optical illumination. sMIM is a non-contact, near-field method able to locally probe the dielectric properties, i.e., the local permittivity and conductivity. The main components of the instrumental setup are shown in Scheme 1, with a focus on the tip-sample interaction. For sMIM, a shielded cantilever probe is mounted on an atomic force microscopy (AFM) machine and placed in contact with the sample of interest. The shielded tip is connected via an impedance-matched transmission line to a microwave generator (∼3 GHz) to allow optimal transmission of the microwaves to the tip apex. The microwaves arriving at the tip result in an evanescent field, interacting with the sample near the tip apex. The admittance (reciprocal of impedance) between the sample and tip apex, Y_{ts}, perturbs this impedance-matched system as a function of the local permittivity and conductivity of the sample. The tip-sample admittance influences the phase and amplitude of the reflected microwaves back to the microwave coupler, where its reflected signal is isolated from its incident signal. Next, the reflected signal is subtracted from its incident signal so that only the result of the tip-sample admittance is amplified. Finally, the signal is demodulated in in-phase and out-of-phase components with a phase adjustment obtained during the calibration process. The in-phase signal is denoted as the real part of the signal yielding the MIM-Re images, while the out-of-phase signal is denoted as the imaginary part of the signal yielding the MIM-Im images.[22–26]

Previous measurements using sMIM predominantly focused on the effects of degradation due to light, air, or a combination of both.[23,27,28] Here, we want to examine the charge concentration over the surface of two MHPs, i.e., $Cs_{0.17}FA_{0.83}PbI_3$ (hereafter denoted as $CsFAPbI_3$) and $MAPbI_3$. We study these materials by comparing the MIM-Re and MIM-Im images recorded in the dark and under optical excitation using a green power LED at 530 nm. While in the dark the MIM-Re images show no contrast, with increasing light intensities, the contrast increases. By converting the individual pixels comprising the MIM-Re images into a histogram, apart from a

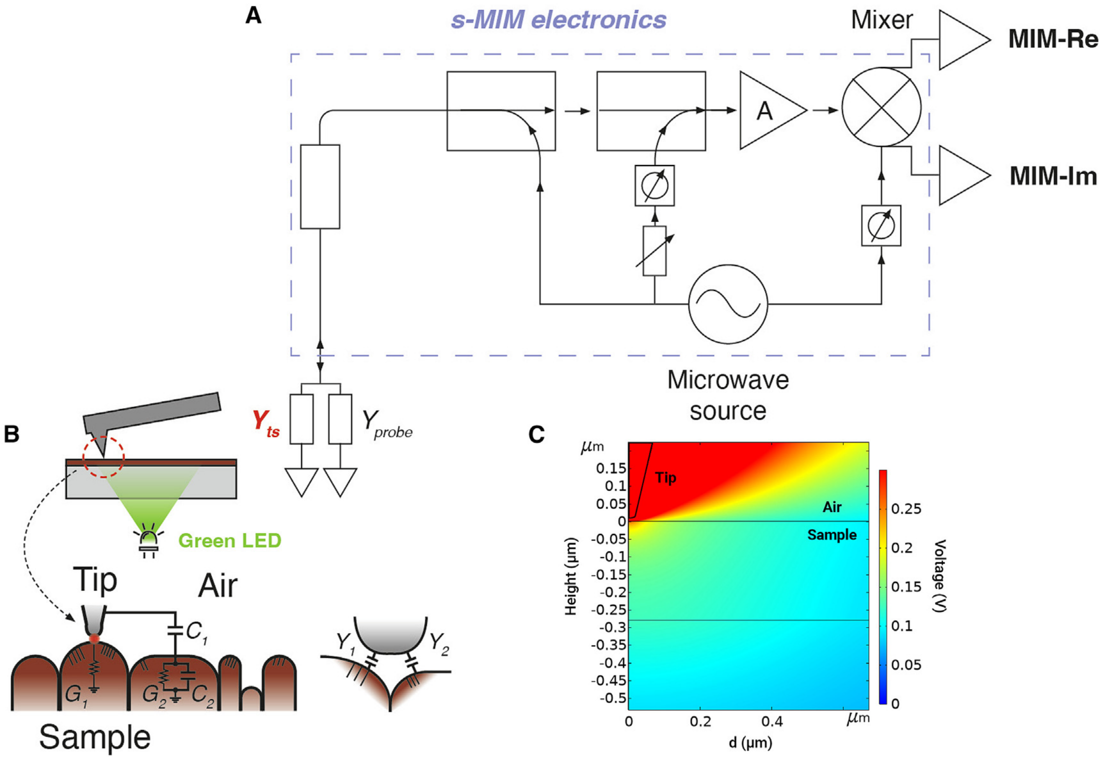

Scheme 1. Illustrations of the sMIM setup and the tip-sample interaction

(A) Main components of the commercial sMIM instrumental setup.

(B) Interaction between the scanning tip and the topology/dielectric properties of the crystalline grains of the sample surface. The illumination system used in this work (green LED) is also shown.

(C) The size of the evanescent microwave electric field at the tip-sample contact region, illustrating the penetration depth within the sample probed by the microwaves.

broadening, a shift is also observed for both MHPs with increasing light intensity. From here, we conclude that, in particular for $MAPbI_3$, the charge carrier distribution is rather homogeneous. For $CsFAPbI_3$, illumination leads to additional contrast over a single grain, which we associate with the fact that $CsFAPbI_3$ shows a non-preferential orientation growth. Various crystal facets with different surface terminations have an effect on the defect density and thus on the excess charge concentration. Hence, for a $CsFAPbI_3$ layer featuring various planes possibly within a grain, the variation in excess charge concentration leads to more contrast, even over a single grain. This insight highlights the need for a homogeneous, preferential growth of the MHP absorber layer in order to prevent heterogeneities in charge carrier distribution and the associated voltage deficit in perovskite solar cells.

RESULTS AND DISCUSSION

Perovskite synthesis and characterization

For our sMIM studies, around 500-nm-thick layers of $CsFAPbI_3$ and 300 nm $MAPbI_3$ were deposited on quartz substrates by spin coating from either mixed DMF/DMSO or pure DMF precursor solution. For deposition of $CsFAPbI_3$, anisole was used as an anti-solvent (see Note S1 for more details). The X-ray diffraction (XRD) patterns shown in Figure S1 disclose a very high preferential growth for $MAPbI_3$, while for $CsFAPbI_3$, a more randomly orientated polycrystalline layer is observed. The use of the anti-solvent forcing quick precipitation and crystallization could, for $CsFAPbI_3$, explain the absence of preferential growth. In Figure S2, the optical

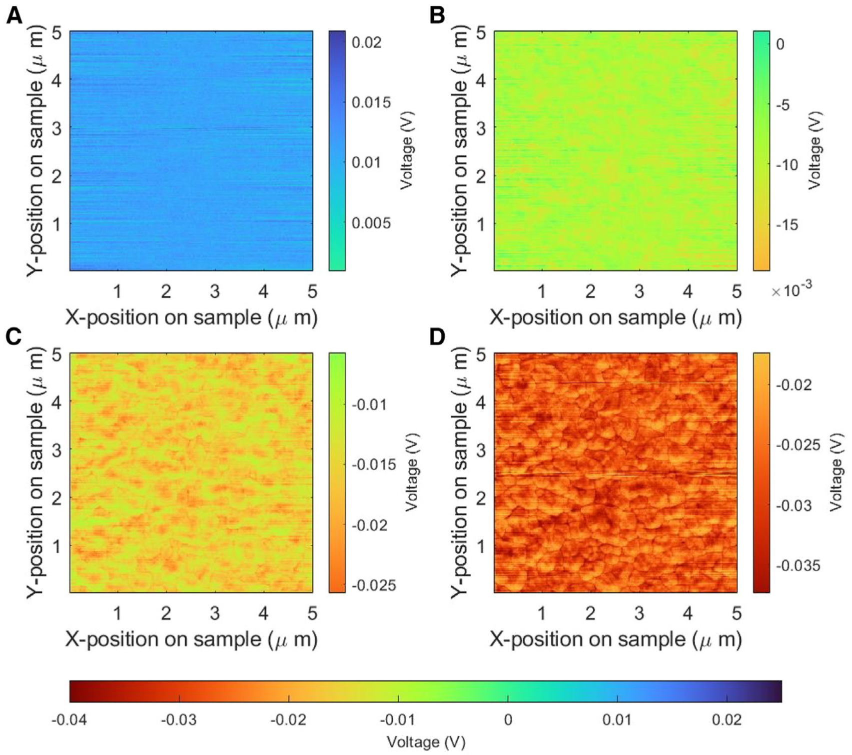

Figure 1. The MIM-Re images of CsFAPbI$_3$ measured in the dark and under illumination
(A) 0, (B) 23.9, (C) 52.3, and (D) 85.3 mW/cm^2 at a wavelength of λ = 530 nm.

attenuation of both samples is provided, showing optical absorption onsets in line with the literature.[29,30]

sMIM

Next, we measured the MIM-Re and MIM-Im images of the CsFAPbI$_3$ layer in the dark and at gradually higher light intensities (see Figure 1). During the measurements, the perovskite sample is illuminated from the backside. This *in situ* illumination setup consists of a power LED with a wavelength of 530 nm, which illuminates the center area of about 3 mm^2 of the sample homogeneously (see Scheme 1B). It is worth noting that the system stabilization time takes approximately 10 min, and hence the charge carrier distribution in the sample is already in a steady-state condition under illumination when the measurement is performed. In Note S2 and Figures S3 and S4, the experimental methods including the used corrections are described in detail. Most importantly, the MIM-Re images show, in the dark, hardly any contrast, while with gradually higher light intensities, two important observations can be made. First, the contrast increases, and second, the mean voltage of the entire image changes, which is apparent from the change in color. These changes in the MIM-Re image are a direct result of the light-induced excess charges that are created by the green LED. Basically, these excess charges can be accelerated by the evanescent microwave field produced at the sMIM tip apex, which leads to some microwave power dissipation and hence a reduction in reflected microwave power. The MIM-Im images recorded at different light intensities are rather comparable, as shown in Figure S5, apart from a small reduction in the average voltage. It is important to note here that the sMIM images do not have a direct resemblance to the surface topology but result from the interaction of the evanescent field present at the cone-shaped tip with the non-planar surface of the sample (see Scheme 1C).

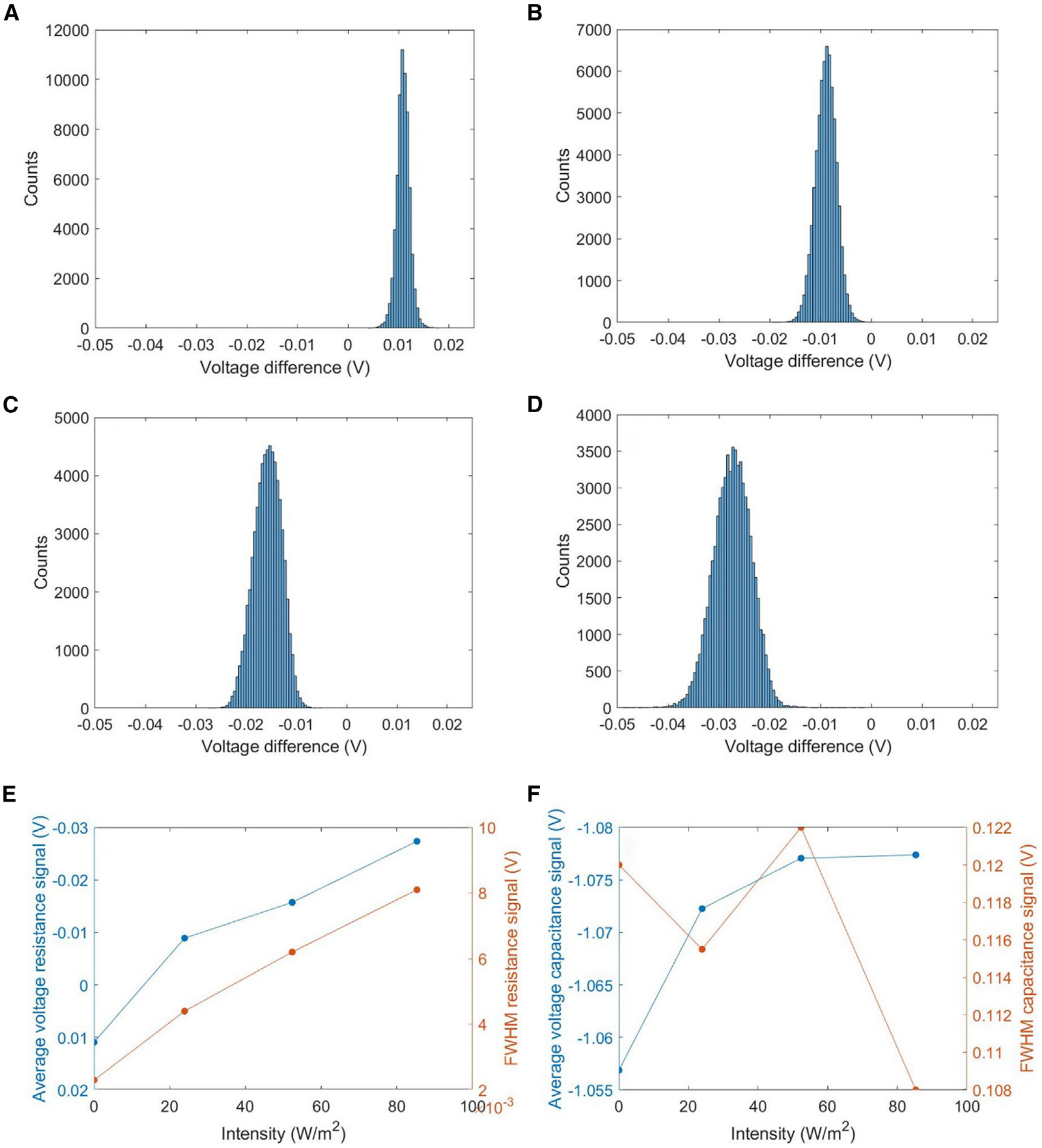

Figure 2. Analysis of histograms derived from MIM-Re images for $CsFAPbI_3$ recorded at various light intensities

(A–D) 0 (A), 23.9 (B), 52.3 (C), and 85.3 mW/cm^2 (D) at a wavelength of λ = 530 nm.

(E) The dependence of the average voltage (V_{avg}; blue) and the full width at half maximum of the histogram (V_{FWHM}; orange) representing, respectively, the mean and the contrast of the MIM-Re image vs. the used light intensity are presented.

(F) The same dependencies as (E) for the MIM-Im images.

To extract more quantitative information from the acquired MIM-Re and MIM-Im images, all data points constituting the MIM-Re image were analyzed by making the histograms shown in Figures 2A–2D. Note that for the histograms, the voltage of the raw data points is used to obtain a full picture of the light-induced changes within the MHP layer. Here, two interesting observations can be made for the MIM-Re data as shown in Figure 2. First, the average value of the data points (V_{avg}) shifts gradually to lower values. On top of that, the full width at half maximum values (V_{FWHM}) of the histograms become larger, meaning that a stronger contrast is observed. However,

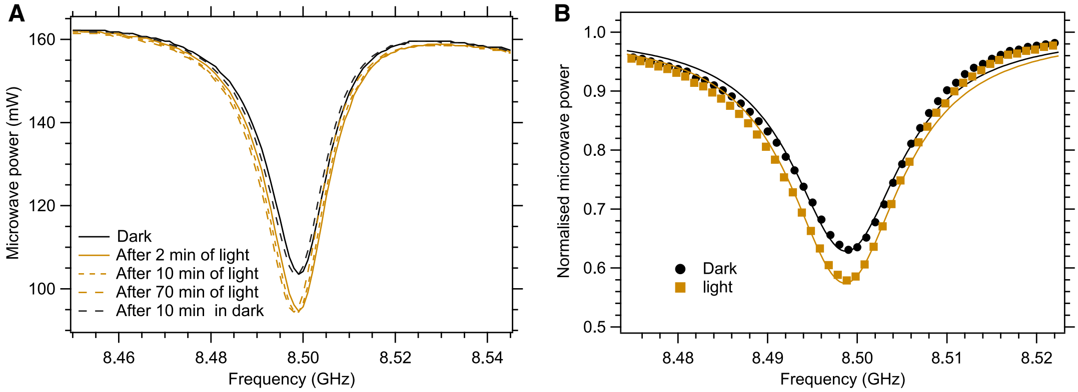

Figure 3. Experimentally recorded steady-state microwave frequency spectra

(A) SSMC measurements for $CsFAPbI_3$ at different illumination times. From fitting (full lines) the normalized SSMC spectra (markers) in the light and in the dark, (B) a light-induced conductance of 1.15 μS is deduced (corresponding to a conductivity of 1 S/m).

V_{avg} and V_{FWHM} derived from the MIM-Im images hardly change, as shown in Figure S6.

Upon plotting V_{avg} and V_{FWHM} of the MIM-Re image as a function of the light intensity, we observe similar trends as shown in Figure 2E. This implies that the higher the conductivity, the more contrast can be discerned. As mentioned, little variation is observed for the contrast for the MIM-Im images, which is confirmed by small variations of V_{FWHM} shown in Figure 2F. Very similar results were obtained for other perovskites such as $MAPbI_3$, showing that only in the presence of excess carriers is contrast in the MIM-Re image visible (see Figure S7). On the contrary, for $CsFAPb(I_{0.6}Br_{0.4})_3$, no contrast could be recorded in the MIM-Re image upon light exposure. This can be attributed to the short lifetimes of the excess charge carriers in this material, leading to low photoconductivities.[31]

Steady-state microwave conductance

Next, to make an estimate of the size of light-induced conductance, another microwave-based technique, i.e., SSMC was applied. This method, relying on the interaction of microwaves with free mobile carriers, allows for determining the conductivity of thin films in an electrodeless fashion.[32] The working principle and instrumental setup are described in the supplemental information (Figure S8). Figure 3A shows the frequency scans of $CsFAPbI_3$ in dark and light of comparable intensity as used in the sMIM measurements. In the absence of light, the frequency scan resembles the scan of an identical quartz substrate, demonstrating the intrinsic nature of the pristine material in the dark. Upon light exposure, the dip of the frequency scan deepens more or less independent of the illumination time. Switching off the light source yields a scan identical to the original intrinsic material. In Figure 3B, quantitative analyses on the frequency scans are performed to reveal the light-induced conductivity amounting to 1.6 S/m for the 500-nm-thick $CsFAPbI_3$ layer (see Note S3 for more detailed information).[32] This is comparable to the conductivity found in $MAPbI_3$, while for $CsFAPb(I_{0.6}Br_{0.4})_3$, values are substantially smaller. From here, we can conclude that conductivities in the order of 1 S/m in the sample under investigation are required to obtain appreciable contrast in the MIM-Re image.

Modeling

Next, we want to examine what kind of response such a conductivity change induces in the MIM-Re and MIM-Im images on a theoretical basis. Therefore, changes in

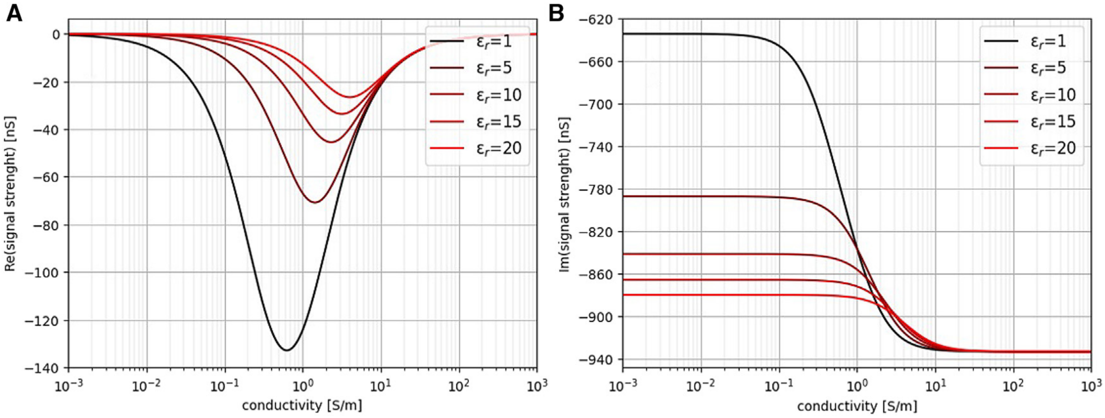

Figure 4. Calculated in- and out-of-phase microwave response as a function of conductivity using finite-element calculations

(A) The MIM-Re and (B) MIM-Im signals as functions of the conductivity of the layer. The various lines represent the responses for different relative permittivity values. A tip-sample distance of 2 nm is assumed in the calculations.

admittances are calculated as a function of the conductivity of the sample for various values of the permittivity using a finite-element analysis method (see Note S2 for the used method).

Figure 4A shows how the in-phase microwave reflection intensity, responsible for the MIM-Re image, is a function of the conductivity of the perovskite layer. Changing the relative permittivity leads to different signal strengths, while the maximum response also changes slightly to a higher conductivity value. However, basically, an appreciable response can be expected around conductivity values close to 1 S/m, which are comparable to previously reported values using this theoretical approach.[23],[27] This perfectly aligns with our previous discussion, in which we concluded that for observing contrast in the MIM-Re image, conductivities in this order of magnitude are required. Moreover, at low conductivities, the signal strength is basically zero, and no contrast can be observed.

Next, we calculated the microwave reflection for the out-of-phase signal related to the MIM-Im image as a function of the perovskite conductivity (see Figure 4B). Since even at low conductivities, the out-of-phase signal is non-zero, a MIM-Im image can be expected in line with our observations. Clearly, variations in the relative permittivity lead to changes in the observed contrast. Variations in the permittivity can be expected to occur near or at grain boundaries.[33] At higher conductivities, the reflection becomes independent of the permittivity and, at some point, even independent of conductivity variations. Most importantly, an increase in the conductivity up to about 1 S/m will give rise to a different signal strength not only in the MIM-Re image but also in the MIM-Im image.

Charge carrier distribution under illumination

In the next part, we look in detail at the changes appearing in the sMIM images upon switching from dark to light. Basically, this means that we go from a low <0.1 S/m to an overall conductivity of about 1.6 S/m as revealed by the SSMC measurements. As discussed in the introduction, we want to investigate to what extent the corresponding charge carriers distribute homogeneously over the grains. To this end, we will investigate the changes induced by visible light by comparing both MIM-Re and MIM-Im images with the topological images shown in Figure 5 for $CsFAPbI_3$. Histograms derived from the sMIM images are provided in Figure S9. Optical excitation of

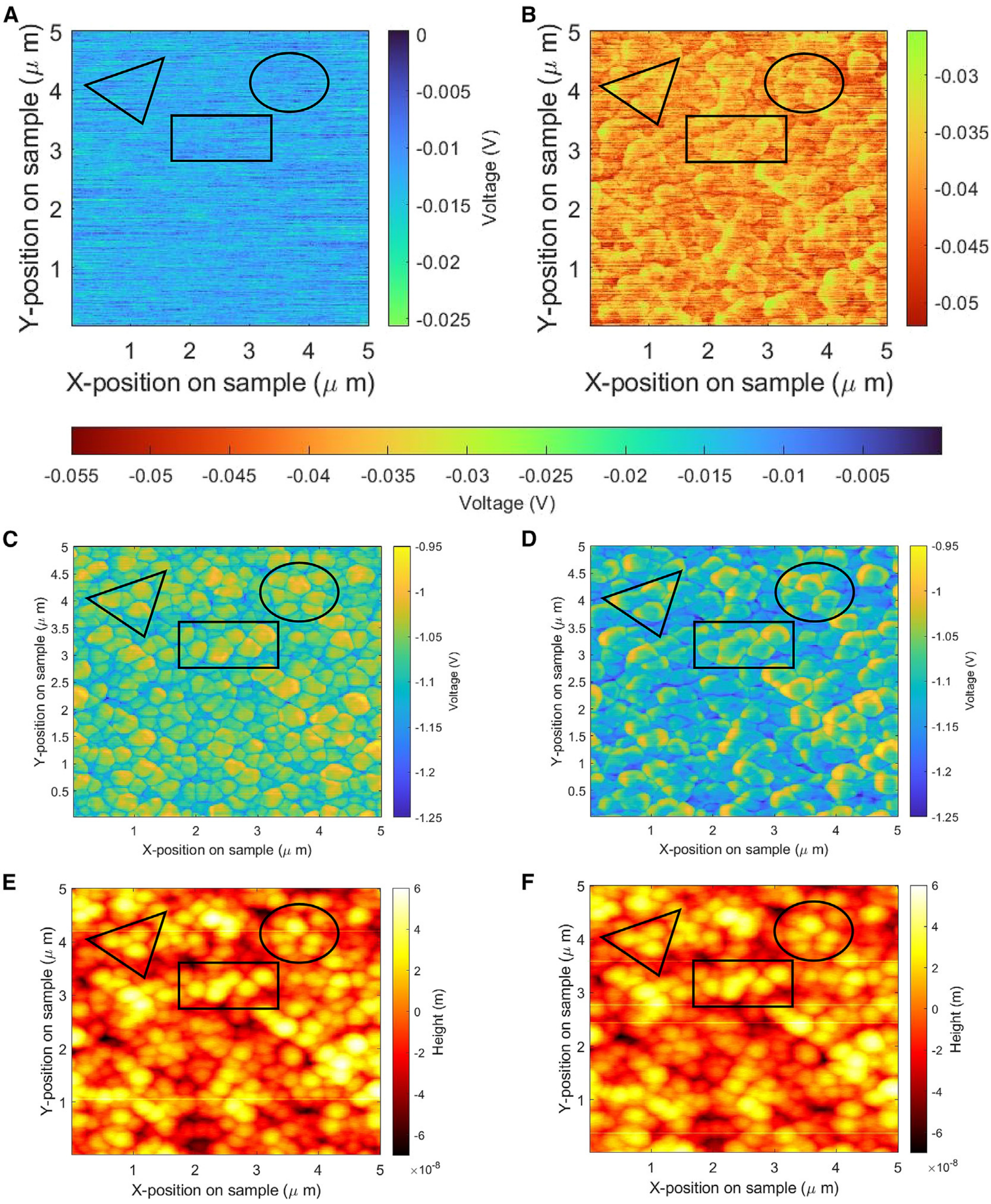

Figure 5. Comparison of MIM-Re, MIM-Im, and topology in the dark and under illumination

(A and B) MIM-Re, (C and D) MIM-Im, and (E and F) topological images of $CsFAPbI_3$ measured in the dark (left) and upon exposure with monochromatic light of 85.3 mW/cm^2 at λ = 530 nm (right). The markers are used to illustrate the correlations between the MIM images and topology.

the perovskite leads to similar changes in the V_{avg} and FWHM values of the MIM-Re image as those for the highest intensity used in Figure 1D. Furthermore, we want to add here that upon continuing to record multiple images (>10) during illumination, the V_{avg} remains constant, indicating that no degradation of optoelectronic properties of the perovskite occurs during the measurement. Images recorded by starting scanning from opposite sites on the MHP surface provide comparable results. Furthermore, the illuminated spot does not show any signs of phase changes or formation of PbI_2 upon illumination, as derived from XRD after optical excitation (see

Figure S10). The MIM-Im image in the dark provides detailed information regarding the grain dimensions constituting the perovskite layer. The individual grains are relatively homogeneous in appearance. Corresponding grains can, to some extent, be identified in the topological images, which are illustrated by the different markers in Figures 5E and 5F, although the resolution of the latter images is limited. Then, upon illumination, the topological image remains basically identical, as shown by the identical features indicated by the markers, although some blunting of the tip might lead to some reduction of fine contrast. Interestingly, when inspecting the MIM-Im image upon illumination, the individual grains reveal substantially more variation, as denoted in Figure 5D. In particular, in the areas near the grain boundaries, more contrast is visible. Hence, upon comparing the MIM-Im images in the light and the dark, we can conclude that for $CsFAPbI_3$, the charge distribution is not only influenced by the morphology but also other factors that influence the charge distribution under illumination. Upon comparing the MIM-Re and MIM-Im images recorded in the light, corresponding areas can be recognized, although the MIM-Re image shows less resolution.

To see whether these effects also occur in other MHPs, sMIM and topologic images of $MAPbI_3$ are recorded in the dark and in the light (see Figures S11 and S12). The grain sizes of $MAPbI_3$ are clearly larger than those of $CsFAPbI_3$. The histograms for the MIM-Re image show, upon illumination, a clear shift, comparable to that of $CsFAPbI_3$. Although the MIM-Im images show, in the dark, comparable features to $CsFAPbI_3$, upon optical excitation, the MIM-Im images of $MAPbI_3$ lack the enhanced contrast near the grain boundaries. To quantitatively substantiate the claims above, we plotted the voltages of the MIM-Im image vs. the height from the topological images of $MAPbI_3$ and $CsFAPbI_3$ measured in the dark and under illumination (see Figures S13). To monitor the correlation between MIM-Im and topology, we linearly fitted the data and obtained a value of R^2, which allows for the evaluation of the quality of the fit. Most importantly, the R^2 values of $MAPbI_3$ in the dark (Figure S13A) and upon light exposure (Figure S13B) are very comparable, implying that, upon illumination, the charge distribution in $MAPbI_3$ does not vary much. This is in agreement with the visual observations that the individual grains of $MAPbI_3$ appear relatively homogenously upon illumination. In contrast, for $CsFAPbI_3$, the R^2 upon illumination is substantially smaller than the R^2 found in the dark. From the correlation plots, we can conclude that for $CsFAPbI_3$, the charge distribution is not only influenced by the morphology but also other factors influence the charge distribution of excess carriers.

We now turn to the question of how excess charge carriers distribute upon illumination. Firstly, it is important to realize that by looking at the histograms of Figures S9 for $CsFAPbI_3$ and S11 for $MAPbI_3$, the V_{avg} has shifted substantially, and no overlap between histograms with or without light is present. This implies that light-induced charges are spread over entire grains. This is also visualized by the complete color change in Figures 5 and S12. As detailed in the modeling section, enhanced conductivity might essentially give rise to more contrast in the MIM-Re image; however, the signal strength is also always modulated by the permittivity and topology. For the MIM-Im image, contrast is a result of variation of the polarizability and topology, but the conductivity also has an impact. Hence, we tentatively attribute the enhanced contrast in the MIM-Im image near the grain boundaries within the individual grains for the $CsFAPbI_3$ to areas with a high density of trap states and/or excess charges. Since similar features are also discernable in the MIM-Re image, it is more likely that we have local areas with increased carrier concentration present in this location. In short, the sMIM images for $CsFAPbI_3$ reveal that charges are distributed evenly over the grains but that local perturbation in carrier concentration around these local defect-rich areas exists. This would suggest that the defective areas with higher charge carrier concentrations are missing in $MAPbI_3$. A possible explanation might be found in the very high preferential growth of the $MAPbI_3$ grains, which is absent for $CsFAPbI_3$ as revealed by the XRD measurements. Since the surface terminations for different crystal planes are chemically different, this will have an effect on the defect density and thus on the excess charge concentration.[34,35] Hence, for a $CsFAPbI_3$ layer exhibiting a highly non-preferential growth, we can expect different crystal facets on the surface of a grain, which leads to a variation in excess charge concentration and hence more contrast over a single grain.

The above observations bring us back to the original question, namely how the excess charge carriers are distributed over the perovskite layer. A straightforward conclusion is that polycrystalline MHP layers comprising randomly orientated grains with different surface terminations show variation in excess charge carriers. This conclusion seems to be in line with previous research using locally recorded I/V curves using photoconductive AFM. In that work, differences in photovoltage and -current were linked to dissimilarities in crystal facets leading to different charge carrier dynamics.[18] In fact, the present findings also agree with the previous statements that grains might comprise multiple smaller grains with varying crystal orientations.[19,20] As mentioned in the introduction, the excess charge carrier concentration directly determines the Fermi level splitting. Thus, variations in Fermi level splitting over the MHP surface will lead to a voltage loss. A way to avoid this might be trying to achieve a more homogeneous grain crystallization during depositions such that the interface with the transport layer is microstructurally and chemically more uniform. Alternatively, another viable solution may be studying passivation treatments targeting the most vulnerable surface terminations. This will avoid variations in the Fermi level splitting and ultimately improve the PCE.

To conclude, MHPs have demonstrated great potential for various electronic applications including solar cells. High-quality layers containing small concentrations of trap states can be deposited using wet-chemical deposition techniques. In this work, we studied how light-induced excess charge carriers become distributed over such polycrystalline material since this might limit the ultimate voltage of a corresponding photovoltaic device. Here, we have examined the local conductive properties of a $CsFAPbI_3$ and a $MAPbI_3$ layer by using sMIM in the dark and upon optical excitation. With gradually increasing optical intensities, both the measured averaged signal height as well as the contrast increase in the MIM-Re images. We conclude that a conductivity on the order of 1 S/m is required for recording an appreciable MIM-Re image, in line with modeling. Interestingly, in the MIM-Im image for $CsFAPbI_3$ the individual grains reveal substantially more variation in illumination than in the dark, in particular in areas near the grain boundaries. This effect is missing for the MIM-Im image of $MAPbI_3$. We attribute this observation to the very high preferential growth of the $MAPbI_3$ grains, which is absent for $CsFAPbI_3$ as revealed by the XRD measurements. Since the surface terminations for different crystal planes are chemically different, this will have an effect on the defect density and thus on the excess charge carrier concentration. Combining the information from both microwave and topological images leads to a picture in which excess charges are distributed evenly over the grains, but a local perturbation in carrier concentration exists due to local defect-rich areas. For solar cells, this spread in carrier concentration under illumination leads to variation in the local Fermi level splitting and should be suppressed efficiently. This insight highlights the need for a homogeneous, preferential growth of the MHP absorber layer to enhance to attainable open circuit voltage of a corresponding solar cell.

EXPERIMENTAL PROCEDURES

Resource availability

Lead contact

Further information and requests for resources and materials should be directed to and will be fulfilled by the lead contact, Tom J. Savenije (T.J.Savenije@tudelft.nl).

Materials availability

All reagents and solvents are available commercially and were used directly without further treatment. PbI_2 (99.999%) was purchased from Alfa Aesar. FAI (99.99%) and MAI (99.99%) were purchased from Greatcell Solar. $PbAc_2 \cdot 3H_2O$ (99.999%) and CsI (99.999%) were purchased from Merck Sigma. DMF (anhydrous, 99.8%), DMSO (anhydrous, 99.9%), and Anisole (anhydrous, 99.7%) were purchased from Merck Sigma.

Data and code availability

This study did not generate datasets and code.

SUPPLEMENTAL INFORMATION

Supplemental information can be found online at https://doi.org/10.1016/j.xcrp.2023.101491.

ACKNOWLEDGMENTS

Allard Katan is acknowledged for fruitful discussions. J.Z. acknowledges the CSC (China Scholarship Council) for funding, file no. 201906360169.

AUTHOR CONTRIBUTIONS

Conceptualization, T.J.S.; methodology, V.M.v.d.W., J.T., and M.B.; validation, J.S.K.; investigation, V.M.v.d.W. and J.Z.; writing – original draft, T.J.S.; writing – review & editing, J.Z., V.M.v.d.W., J.S.K., J.N., and T.J.S.

DECLARATION OF INTERESTS

The authors declare no competing interests.

Received: March 15, 2023
Revised: May 10, 2023
Accepted: June 14, 2023
Published: July 6, 2023

REFERENCES

1. Zhao, J., Zhao, L., Deng, Y., Xiao, X., Ni, Z., Xu, S., and Huang, J. (2020). Perovskite-filled membranes for flexible and large-area direct-conversion X-ray detector arrays. Nat. Photonics *14*, 612–617. https://doi.org/10.1038/s41566-020-0678-x.
2. Chu, S., Chen, W., Fang, Z., Xiao, X., Liu, Y., Chen, J., Huang, J., and Xiao, Z. (2021). Large-area and efficient perovskite light-emitting diodes via low-temperature blade-coating. Nat. Commun. *12*, 147. https://doi.org/10.1038/s41467-020-20433-4.
3. Yoo, J.J., Seo, G., Chua, M.R., Park, T.G., Lu, Y., Rotermund, F., Kim, Y.K., Moon, C.S., Jeon, N.J., Correa-Baena, J.P., et al. (2021). Efficient perovskite solar cells via improved carrier management. Nature *590*, 587–593. https://doi.org/10.1038/s41586-021-03285-w.
4. Li, Z., Li, B., Wu, X., Sheppard, S.A., Zhang, S., Gao, D., Long, N.J., and Zhu, Z. (2022). Organometallic-functionalized interfaces for highly efficient inverted perovskite solar cells. Science *376*, 416–420. https://doi.org/10.1126/science.abm8566.
5. NREL (2023). Best Research-Cell Efficiencies: Rev. 24-01-2023. Best Res. Effic. Chart, Photovolt. Res.. https://www.nrel.gov/pv/cell-efficiency.html.
6. Yin, W.J., Shi, T., and Yan, Y. (2014). Unique properties of halide perovskites as possible origins of the superior solar cell performance. Adv. Mater. *26*, 4653–4658. https://doi.org/10.1002/adma.201306281.
7. Kim, G.W., and Petrozza, A. (2020). Defect Tolerance and Intolerance in Metal-Halide

Perovskites. Adv. Energy Mater. *10*, 2001959. https://doi.org/10.1002/aenm.202001959.

8. Guo, Y., Wang, Q., and Saidi, W.A. (2017). Structural stabilities and electronic properties of high-angle grain boundaries in perovskite cesium lead halides. J. Phys. Chem. C *121*, 1715–1722. https://doi.org/10.1021/acs.jpcc.6b11434.
9. Guo, D., Caselli, V.M., Hutter, E.M., and Savenije, T.J. (2019). Comparing the calculated fermi level splitting with the open-circuit voltage in various perovskite cells. ACS Energy Lett. *4*, 855–860. https://doi.org/10.1021/acsenergylett.9b00431.
10. Wolff, C.M., Caprioglio, P., Stolterfoht, M., and Neher, D. (2019). Nonradiative Recombination in Perovskite Solar Cells: The Role of Interfaces. Adv. Mater. *31*, e1902762. https://doi.org/10.1002/adma.201902762.
11. Luo, D., Su, R., Zhang, W., Gong, Q., and Zhu, R. (2019). Minimizing non-radiative recombination losses in perovskite solar cells. Nat. Rev. Mater. *5*, 44–60. https://doi.org/10.1038/s41578-019-0151-y.
12. Howard, J.M., Lahoti, R., and Leite, M.S. (2020). Imaging Metal Halide Perovskites Material and Properties at the Nanoscale. Adv. Energy Mater. *10*, 1903161. https://doi.org/10.1002/aenm.201903161.
13. Tennyson, E.M., Doherty, T.A.S., and Stranks, S.D. (2019). Heterogeneity at multiple length scales in halide perovskite semiconductors. Nat. Rev. Mater. *4*, 573–587. https://doi.org/10.1038/s41578-019-0125-0.
14. Stranks, S.D. (2021). Multimodal microscopy characterization of halide perovskite semiconductors: Revealing a new world (dis) order. Matter *4*, 3852–3866. https://doi.org/10.1016/j.matt.2021.10.025.
15. DeQuilettes, D.W., Vorpahl, S.M., Stranks, S.D., Nagaoka, H., Eperon, G.E., Ziffer, M.E., Snaith, H.J., and Ginger, D.S. (2015). Impact of microstructure on local carrier lifetime in perovskite solar cells. Science *348*, 683–686. https://doi.org/10.1126/science.aaa5333.
16. Garrett, J.L., Tennyson, E.M., Hu, M., Huang, J., Munday, J.N., and Leite, M.S. (2017). Real-Time Nanoscale Open-Circuit Voltage Dynamics of Perovskite Solar Cells. Nano Lett. *17*, 2554–2560. https://doi.org/10.1021/acs.nanolett.7b00289.
17. Toth, D., Hailegnaw, B., Richheimer, F., Castro, F.A., Kienberger, F., Scharber, M.C., Wood, S., and Gramse, G. (2020). Nanoscale Charge Accumulation and Its Effect on Carrier Dynamics in Tri-cation Perovskite Structures. ACS Appl. Mater. Interfaces *12*, 48057–48066. https://doi.org/10.1021/acsami.0c10641.
18. Leblebici, S.Y., Leppert, L., Li, Y., Reyes-Lillo, S.E., Wickenburg, S., Wong, E., Lee, J., Melli, M., Ziegler, D., Angell, D.K., et al. (2016). Facet-dependent photovoltaic efficiency variations in single grains of hybrid halide perovskite. Nat. Energy *1*, 16093–16097. https://doi.org/10.1038/nenergy.2016.93.
19. Li, W., Yadavalli, S.K., Lizarazo-Ferro, D., Chen, M., Zhou, Y., Padture, N.P., and Zia, R. (2018). Subgrain special boundaries in halide perovskite thin films restrict carrier diffusion. ACS Energy Lett. *3*, 2669–2670. https://doi.org/10.1021/acsenergylett.8b01704.
20. Jariwala, S., Sun, H., Adhyaksa, G.W., Lof, A., Muscarella, L.A., Ehrler, B., Garnett, E.C., and Ginger, D.S. (2019). Local Crystal Misorientation Influences Non-radiative Recombination in Halide Perovskites. Joule *3*, 3048–3060. https://doi.org/10.1016/j.joule.2019.09.001.
21. Doherty, T.A.S., Winchester, A.J., Macpherson, S., Johnstone, D.N., Pareek, V., Tennyson, E.M., Kosar, S., Kosasih, F.U., Anaya, M., Abdi-Jalebi, M., et al. (2020). Performance-limiting nanoscale trap clusters at grain junctions in halide perovskites. Nature *580*, 360–366. https://doi.org/10.1038/s41586-020-2184-1.
22. Coakley, K.J., Berweger, S., Wallis, T.M., and Kabos, P. (2019). Disentangling topographic contributions to near-field scanning microwave microscopy images. Ultramicroscopy *197*, 53–64. https://doi.org/10.1016/j.ultramic.2018.11.003.
23. Chu, Z., Yang, M., Schulz, P., Wu, D., Ma, X., Seifert, E., Sun, L., Li, X., Zhu, K., and Lai, K. (2017). Impact of grain boundaries on efficiency and stability of organic-inorganic trihalide perovskites. Nat. Commun. *8*, 2230–2238. https://doi.org/10.1038/s41467-017-02331-4.
24. Rubin, K.A., Yang, Y., Amster, O., Scrymgeour, D.A., and Misra, S. (2019). Electrical Atomic Force Microscopy for Nanoelectronics: Scanning Microwave Impedance Microscopy (sMIM). In Electronic and Quantum Materials, U. Celano, ed. (NanoScience and Technology). https://doi.org/10.1007/978-3-030-15612-1_1.
25. Lai, K., Kundhikanjana, W., Kelly, M.A., and Shen, Z.X. (2011). Nanoscale microwave microscopy using shielded cantilever probes. Appl. Nanosci. *1*, 13–18. https://doi.org/10.1007/s13204-011-0002-7.
26. Lai, K., Kundhikanjana, W., Kelly, M., and Shen, Z.X. (2008). Modeling and characterization of a cantilever-based near-field scanning microwave impedance microscope. Rev. Sci. Instrum. *79*, 063703. https://doi.org/10.1063/1.2949109.
27. Berweger, S., MacDonald, G.A., Yang, M., Coakley, K.J., Berry, J.J., Zhu, K., DelRio, F.W., Wallis, T.M., and Kabos, P. (2017). Electronic and Morphological Inhomogeneities in Pristine and Deteriorated Perovskite Photovoltaic Films. Nano Lett. *17*, 1796–1801. https://doi.org/10.1021/acs.nanolett.6b05119.
28. Berweger, S., Zhang, F., Larson, B.W., Ferguson, A.J., Palmstrom, A.F., Reid, O.G., Wallis, T.M., Zhu, K., Berry, J.J., Kabos, P., and Nanayakkara, S.U. (2022). Nanoscale Photoexcited Carrier Dynamics in Perovskites. J. Phys. Chem. Lett. *13*, 2388–2395. https://doi.org/10.1021/acs.jpclett.2c00233.
29. Zhang, W., Pathak, S., Sakai, N., Stergiopoulos, T., Nayak, P.K., Noel, N.K., Haghighirad, A.A., Burlakov, V.M., Dequilettes, D.W., Sadhanala, A., et al. (2015). Enhanced optoelectronic quality of perovskite thin films with hypophosphorous acid for planar heterojunction solar cells. Nat. Commun. *6*, 10030. https://doi.org/10.1038/ncomms10030.
30. Knight, A.J., Borchert, J., Oliver, R.D.J., Patel, J.B., Radaelli, P.G., Snaith, H.J., Johnston, M.B., and Herz, L.M. (2021). Halide Segregation in Mixed-Halide Perovskites: Influence of A-Site Cations. ACS Energy Lett. *6*, 799–808. https://doi.org/10.1021/acsenergylett.0c02475.
31. Guo, D., Andaji Garmaroudi, Z., Abdi-Jalebi, M., Stranks, S.D., and Savenije, T.J. (2019). Reversible Removal of Intermixed Shallow States by Light Soaking in Multication Mixed Halide Perovskite Films. ACS Energy Lett. *4*, 2360–2367. https://doi.org/10.1021/acsenergylett.9b01726.
32. Caselli, V.M., Fischer, M., Meggiolaro, D., Mosconi, E., De Angelis, F., Stranks, S.D., Baumann, A., Dyakonov, V., Hutter, E.M., and Savenije, T.J. (2019). Charge Carriers Are Not Affected by the Relatively Slow-Rotating Methylammonium Cations in Lead Halide Perovskite Thin Films. J. Phys. Chem. Lett. *10*, 5128–5134. https://doi.org/10.1021/acs.jpclett.9b02160.
33. Wilson, J.N., Frost, J.M., Wallace, S.K., and Walsh, A. (2019). Dielectric and ferroic properties of metal halide perovskites. Apl. Mater. *7*, 010901. https://doi.org/10.1063/1.5079633.
34. Oner, S.M., Sezen, E., Yordanli, M.S., Karakoc, E., Deger, C., and Yavuz, I. (2022). Surface Defect Formation and Passivation in Formamidinium Lead Triiodide (FAPbI3) Perovskite Solar Cell Absorbers. J. Phys. Chem. Lett. *13*, 324–330. https://doi.org/10.1021/acs.jpclett.1c03645.
35. Feng, Q., and Nan, G. (2022). How Do A-Site Cations Regulate Trap States at Defective Surfaces of Lead Iodide Perovskites? J. Phys. Chem. Lett. *13*, 4831–4839. https://doi.org/10.1021/acs.jpclett.2c01149.